RSC Advances

PAPER

View Article Online
View Journal | View Issue

Cite this: *RSC Adv.*, 2018, **8**, 1398

Mesoporous TiO_2 coated $ZnFe_2O_4$ nanocomposite loading on activated fly ash cenosphere for visible light photocatalysis†

Hougang Fan,[abc] Dandan Chen,[a] Xuefeng Ai,[a] Shuo Han,[c] Maobin Wei,[abc] Lili Yang,[abc] Huilian Liu[abc] and Jinghai Yang *[abc]

Several activated fly ash cenosphere (AFAC) supporting TiO_2 coated $ZnFe_2O_4$ ($TiO_2/ZnFe_2O_4$/AFAC) photocatalysts were prepared by sol–gel and hydrothermal methods. These photocatalysts were characterized by X-ray diffraction (XRD), scanning electron microscopy (SEM), transmission electron microscopy (TEM), Fourier transform infrared spectroscopy (FT-IR), UV-vis diffuse reflectance spectroscopy (UV-DRS) and nitrogen adsorption analyses for Brunauer–Emmett–Teller (BET) specific surface area measurements. We found that the main components of spherical AFAC were mullite ($Al_6Si_2O_{13}$) and SiO_2; the crystallite size of the $TiO_2/ZnFe_2O_4$ nanocomposite was less than 10 nm and its specific surface area was 162.18 $m^2\ g^{-1}$. The $TiO_2/ZnFe_2O_4$ nanocomposite had a band-gap of 2.56 eV, which would photodegrade 95% of rhodamine B (RhB) under visible light within 75 min. When hybridized with 0.02 g AFAC, the $TiO_2/ZnFe_2O_4$/0.02 g AFAC photocatalyst with a band-gap of 2.50 eV could remove 97.1% of RhB and be reused three consecutive times with minor decrease in photocatalytic performance. However, the photocatalytic performance decreased to 91.0% on increasing the dosage of AFAC to 0.30 g. The mesoporous structure of all the photocatalysts and the strong adsorption ability of AFAC accounted for the notable performance.

Received 8th October 2017
Accepted 18th December 2017

DOI: 10.1039/c7ra11055c

rsc.li/rsc-advances

1. Introduction

With superior photocatalytic performance, high chemical stability, low cost and low-toxicity, TiO_2 has the potential for applications in environmental purification and solar energy conversion.[1–3] However, the wide band gap of TiO_2 (3.18 eV for anatase), making it absorb no more than 5.0% of sunlight, together with the low quantum efficiency (high recombination rate of photogenerated electron–hole pair) hindered its application.[4–6] To extend the visible light response of TiO_2, increasing efforts have been directed towards the improvement of the photocatalytic activity of TiO_2. Some of these methods are: doping ions, surface modification by noble metals and coupling with photosensitive dye and other semiconductors.[7–11] Among these methods, coupling with other semiconductors could efficiently improve the photocatalytic activity of TiO_2 under visible light irradiation.[12–15] In particular, $ZnFe_2O_4$ has been considered as an interesting coupling semiconductor to TiO_2, which could prevent the transformation of TiO_2 from anatase to rutile.[16,17] In addition, $ZnFe_2O_4$ can absorb sunlight since its band gap was about 1.8 eV.[18,19] Hence, under visible light, the utilization of a $TiO_2/ZnFe_2O_4$ nanocomposite in aqueous suspension has potential applications in wastewater treatment.[18–21] Immobilizing TiO_2 on adsorptive or hydrophobic materials would facilitate the oxygenation process throughout the photocatalytic process.[22–25] Fly ash cenosphere (FAC) is the by-product generated in coal-fired power plants and could be used as a hydrophobic material or floating substrate,[6,26,27] which shows bifunctional properties with adsorption capability in addition to photocatalytic activity in loading semiconductor nanoparticles.[28,29]

In this study, the TiO_2 coated $ZnFe_2O_4$ ($TiO_2/ZnFe_2O_4$) nanocomposite was synthesized by a sol–gel method, and then hybridized with different amounts of AFAC for the first time. Compared with the $TiO_2/ZnFe_2O_4$ nanocomposite, the $TiO_2/ZnFe_2O_4$ loaded on AFAC ($TiO_2/ZnFe_2O_4$/AFAC) photocatalyst exhibited better adsorption activity and photocatalytic activity of removal of RhB under visible light.

2. Experimental

2.1 Materials

Fly ash was obtained from thermal power plants of Lingshou city (Hebei province, China). All reagents including zinc acetate dihydrate ($Zn(CH_3COO)_2 \cdot 2H_2O$), sodium hydroxide (NaOH),

[a]Key Laboratory of Functional Materials Physics and Chemistry of the Ministry of Education, Jilin Normal University, Changchun 130103, PR China. E-mail: jhyang1@jlnu.edu.cn

[b]National Demonstration Center for Experimental Physics Education, Jilin Normal University, Siping 136000, PR China

[c]College of Physics, Jilin Normal University, Siping 136000, PR China

† Electronic supplementary information (ESI) available. See DOI: 10.1039/c7ra11055c

ferric chloride hexahydrate ($FeCl_3 \cdot 6H_2O$), hydrazine hydrate ($N_2H_4 \cdot H_2O$), ethylene glycol ($(CH_2OH)_2$), ethanol (C_2H_5OH), cetyl trimethyl ammonium bromide (CTAB), tetrabutyl titanate (TBOT), isopropanol ($(CH_3)_2CHOH$), nitric acid (HNO_3) and rhodamine B (RhB) used in the experiments were analytical grade (purchased from Sinopharm Chemical Regent Co. Ltd) and used without further purification. Deionized water was used throughout the experiment.

2.2 Synthesis

2.2.1 Activating fly ash. The acquired fly ash (10 g) was activated by 200.0 mL HNO_3 under stirring at 80 °C for 2 h, and then washed with deionized water until the pH of the solution was 7. The particles suspended in the solution were collected and dried in a vacuum oven at 80 °C for 24 h.

2.2.2 Preparation of $ZnFe_2O_4$. The mole ratio of $n(Zn) : n(Fe) = 1 : 2$ of the soluble salts was dissolved in a mixture of ethylene glycol and deionized water solution. This mixture was magnetically stirred for 30 min and named as solution A. A certain amount of NaOH was dissolved in deionized water and mixed with hydrazine hydrate, magnetically stirred for 30 min, and the mixture was labeled as solution B. Solutions A and B were mixed and vigorously stirred for 10 min, with the injection of CTAB; magnetically stirring was continued for 20 min. The reaction mixture was transferred into a 100 mL Teflon-lined stainless steel autoclave and kept at 150 °C for 15 h. The obtained dark green products were washed three times with ethanol and deionized water before being dried at 60 °C for 12 h and then crushed in an agate mortar to obtain $ZnFe_2O_4$ powders.

2.2.3 Photocatalysts preparation. The $TiO_2/ZnFe_2O_4$ nanocomposite was prepared using the sol–gel method. Initially, 34.0 mL TBOT was diluted in 8.5 mL isopropoxide solution under stirring. The mixture was added dropwise into 340 mL water with vigorous stirring and the pH was adjusted to 3 with HNO_3. The mixture was placed in a 500 mL flask and heated in a water bath at 75 °C for 12 h. Finally, pure TiO_2 sol was obtained.[30] Further, 0.35 g $ZnFe_2O_4$ powder was dispersed in 300.0 mL TiO_2 sol in an ultrasonic bath for 30 min. Then, it was dried into a powder in a rotatory evaporator under vacuum at 75 °C. The obtained powder was named as TiO_2 coated $ZnFe_2O_4$ nanocomposite ($TiO_2/ZnFe_2O_4$). The final $TiO_2/ZnFe_2O_4$ loadings on AFAC ($TiO_2/ZnFe_2O_4$/AFAC) photocatalysts were obtained by triturating $TiO_2/ZnFe_2O_4$ powder and AFAC with mass ratio of 1 : 0.02 and 1 : 0.30, respectively.

2.3 Characterization

The crystalline structure of the samples was determined using X-ray diffraction (XRD MAC Science, MXP18, Japan). The morphology of the as-synthesized samples was characterized by field emission scanning electron microscopy (FESEM, JEOL JEM-2010HR) and transmission electron microscopy (TEM, JEOL JEM-2010HR). N_2 adsorption isotherms were measured using an AUTOSORB-IQ (Quantachrome Instruments, USA). UV-vis absorption spectra were acquired with an UV-vis spectrophotometer (UV-5800PC, Shanghai Metash Instruments Co., Ltd).

2.4 Photocatalytic activity test

The photocatalytic performance of the as-prepared photocatalysts was evaluated by the photocatalytic decomposition of rhodamine B (RhB) aqueous solution. In the experiment, 50 mg of the as-prepared photocatalyst was dispersed in 50.0 mL of RhB solution (10 mg L^{-1}) in a 100 mL beaker. A 350 W Xe lamp equipped with a 420 nm cut-off filter was used as a light source along with a cooling device to eliminate the thermal effect. The average light energy density was estimated to be 68 mW cm^{-2}. The distance between the beaker containing the reaction mixture and the light source was fixed at 16 cm. First, the reaction mixture was mechanically stirred for 30 min in the dark to ensure the adsorption/desorption equilibrium of the RhB on the surface of the photocatalysts. The reaction solutions were sampled at 15 min illumination intervals, and the corresponding UV-vis spectra (measured over the range of 300–800 nm) were recorded to monitor the progress of the degradation of RhB using an UV-vis spectrophotometer. All the photocatalytic performances were tested under UV light, visible light and sunlight. To investigate the stability of the $TiO_2/ZnFe_2O_4$/0.02 g AFAC photocatalyst, the composite was reused three times for the photocatalytic degradation of RhB (10 mg L^{-1}).

3. Results and discussion

3.1 Structure and morphology of photocatalysts

Fig. 1 shows the X-ray diffraction patterns of AFAC, $ZnFe_2O_4$, $TiO_2/ZnFe_2O_4$ nanocomposite and the $TiO_2/ZnFe_2O_4$/0.02 g AFAC sample. For the AFAC sample, most diffraction peaks belonged to mullite ($Al_6Si_2O_{13}$, JCPDF no. 15-0776); the amorphous phase located at 22° primarily composed of SiO_2 (JCPDF no. 88-1535). For the as-prepared $ZnFe_2O_4$ sample, all the diffraction peaks belonged to $ZnFe_2O_4$ (JCPDF no. 82-1049). For

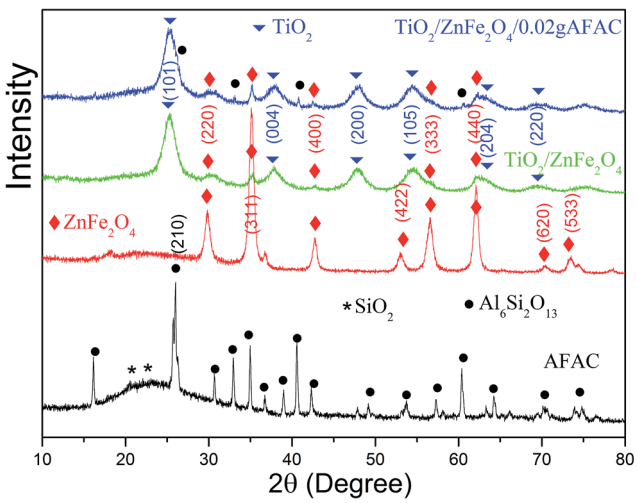

Fig. 1 The XRD spectra of AFAC, $ZnFe_2O_4$, $TiO_2/ZnFe_2O_4$ and $TiO_2/ZnFe_2O_4$/0.02 g AFAC samples.

Table 1 The crystallite size and band gap of different samples

Sample	$ZnFe_2O_4$	$TiO_2/ZnFe_2O_4$	$TiO_2/ZnFe_2O_4$/0.02 g AFAC	$TiO_2/ZnFe_2O_4$/0.30 g AFAC
Crystallite size (nm)	25.0 ± 2.3	8.7 ± 0.6	8.4 ± 0.5	9.1 ± 0.9
Band gap (eV)	1.33	2.56	2.50	2.44

the $TiO_2/ZnFe_2O_4$ nanocomposite, the TiO_2 on the surface of $ZnFe_2O_4$ exhibited a dominant anatase phase (JCPDF no. 84-1286), while five diffraction peaks of $ZnFe_2O_4$ could also be observed at lower intensity, which demonstrated that the amount of $ZnFe_2O_4$ accounted for a small proportion. For the $TiO_2/ZnFe_2O_4$/0.02 g AFAC sample, the diffraction peaks of $Al_6Si_2O_{13}$, $ZnFe_2O_4$ and TiO_2 could all be observed and marked by different symbols. However, the peak intensities of mullite were relatively small, which suggested that the amount of AFAC in the $TiO_2/ZnFe_2O_4$/0.02 g AFAC sample was small. The crystallite sizes of the above samples were determined from the broadening of the corresponding X-ray diffraction peaks by using Scherer's formula $D = (K\lambda)/(\beta \cos \theta)$, where λ is the wavelength of the X-ray radiation ($\lambda = 0.15406$ nm), K is the Scherer constant ($K = 0.9$), θ is the X-ray diffraction peak and β is the full-width at half maximum (FWHM) of the peak (in radians), which was corrected for the instrumental broadening ($\beta_0 = 0.00122$ rad) prior to the calculation of its crystallite size broadening. The crystallite sizes were calculated and listed in Table 1. The crystallite sizes of $TiO_2/ZnFe_2O_4$, $TiO_2/ZnFe_2O_4$/0.02 g AFAC and $TiO_2/ZnFe_2O_4$/0.30 g AFAC samples were all less than 10 nm, which implied that the above samples would have a large specific surface area.

Fig. 2A–C show the SEM and TEM images of AFAC. In Fig. 2A and B we can observe that the particle shape of AFAC was spherical and their diameters ranged from about 1 μm to nearly 10 μm, which was similar to previous studies.[6,26–28] In Fig. 2C, the perfect AFAC sphere is presented in the TEM image with some tiny particles on its surface, which implied that the AFAC had adsorption ability. Fig. 2D shows the SEM image of $ZnFe_2O_4$, whose crystallite size is about 20–30 nm, coinciding with the results summarized in Table 1. Fig. 2E and F represent the SEM and TEM images of the $TiO_2/ZnFe_2O_4$ nanocomposite. It could be observed that the dark $ZnFe_2O_4$ particles with a crystallite size of about 25 nm are coated by the outer grey homogeneous layer of TiO_2 particles with a crystallite size of less than 10 nm, which coincided with the results summarized in Table 1. Fig. 2G and H show the SEM image and EDS results

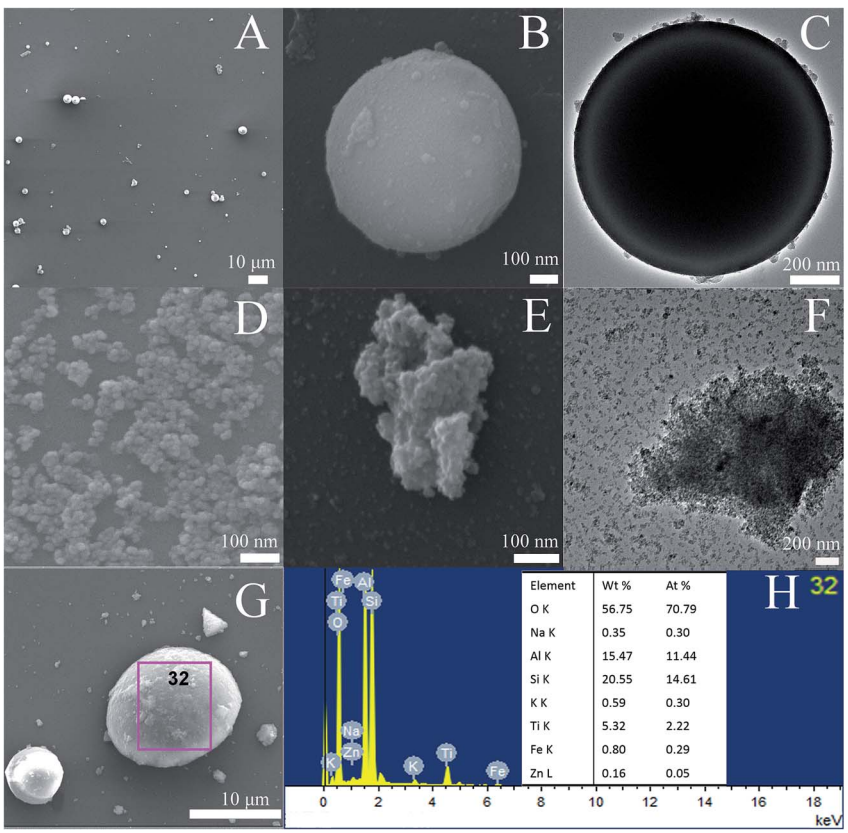

Fig. 2 SEM images (A, B) and TEM image (C) of AFAC, SEM image (D) of $ZnFe_2O_4$, SEM images (E) and TEM image (F) of $TiO_2/ZnFe_2O_4$ nanocomposite, SEM image (G) and EDS (H) of $ZnFe_2O_4/TiO_2$/0.30 g AFAC sample.

of the $ZnFe_2O_4/TiO_2$/0.30 g AFAC sample. It can be observed that the AFAC particle is semi-spherical and the $ZnFe_2O_4/TiO_2$ particles are loaded on the AFAC surface. The EDS elemental analysis shows that most of the elements are oxygen (70%), silicon (14%), aluminum (11%) and titanium (2.3%), which corresponds to the compounds SiO_2, $Al_6Si_2O_{13}$ and TiO_2, respectively. AFAC primarily consisted of SiO_2, $Al_6Si_2O_{13}$, and other oxides, such as Fe_2O_3. Only 0.05% of zinc and 0.29% of iron were found, which corresponded to the compounds Fe_2O_3 and $ZnFe_2O_4$, which might be because the added amount of $ZnFe_2O_4$ was small (3 wt%, wt% is an abbreviation of weight percentage) and the $ZnFe_2O_4$ particles were coated by TiO_2 particles.

3.2 FT-IR spectrum

FT-IR analysis was performed on $TiO_2/ZnFe_2O_4$, $TiO_2/ZnFe_2O_4$/0.02 g AFAC and $TiO_2/ZnFe_2O_4$/0.30 g AFAC composites to further prove the coating of TiO_2 on $ZnFe_2O_4$ and the existence of AFAC. Fig. 3 shows their FT-IR spectra recorded over the range of 4000–500 cm^{-1}. In all the spectra, the band centered at 551 cm^{-1} can be assigned to the Zn–O stretching of $ZnFe_2O_4$ (ref. 31) and the band centered at 1384 cm^{-1} can be attributed to the Ti–O–Ti vibration observed in TiO_2.[32] The band centered at 1630 cm^{-1} can be assigned to the bending vibration of the O–H bond of chemisorbed water,[33] while the band centered at 1053 cm^{-1} in the spectra of the $TiO_2/ZnFe_2O_4$/0.02 g AFAC and $TiO_2/ZnFe_2O_4$/0.30 g AFAC composites could be assigned to the asymmetric stretching of Si–O–Si groups of AFAC,[33] which could not be observed in the spectrum of the $TiO_2/ZnFe_2O_4$ nanocomposite.

3.3 Pore structure and surface area determination

N_2 adsorption measurement was carried out to characterize the porous structures and specific surface area of the $TiO_2/ZnFe_2O_4$, $TiO_2/ZnFe_2O_4$/0.02 g AFAC and $TiO_2/ZnFe_2O_4$/0.30 g AFAC photocatalysts. Fig. 4A–C display the N_2 adsorption–desorption isotherms and the corresponding pore size distribution histogram of the above samples. According to the International Union of Pure and Applied Chemistry (IUPAC) classification, all the samples exhibited reversible type IV isotherms with H3-type hysteresis loop,[34,35] which indicated the formation of mesoporous materials.[36] The hysteresis loop in the relative pressure range between 0.4 and 0.9 was probably related to the finer intra-aggregated pores formed between intra-agglomerated primary particles in the above composites. The pore diameter distribution histogram was calculated using the adsorption branch of the isotherm, which indicated the presence of mesopores (from 30 to 50 nm) and macropores (from 50 to 120 nm). The mesoporous structure could be related to the pores formed between stacked TiO_2 particles coating on the $ZnFe_2O_4$ particles. The data summarized in Table 2 indicated that the BET specific surface area of the above photocatalysts were all more than 150.00 $m^2\ g^{-1}$ and larger than that reported in some previous studies (less than 100.00 $m^2\ g^{-1}$), which inferred that all the composites would have a strong adsorption ability.

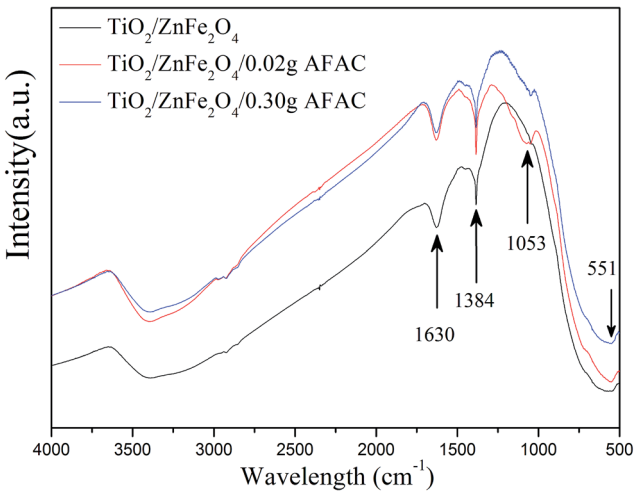

Fig. 3 The FT-IR spectra of $TiO_2/ZnFe_2O_4$, $TiO_2/ZnFe_2O_4$/0.02 g AFAC and $TiO_2/ZnFe_2O_4$/0.30 g AFAC samples.

3.4 UV-vis photoresponse and band gap determination

The UV-vis diffuse reflectance spectra (UV-DRS) of the samples are depicted in Fig. 5. It is clearly shown that the as-prepared $TiO_2/ZnFe_2O_4$/AFAC samples primarily absorbed UV light and part of the visible light. There are three intrinsic adsorption edges located at 380 nm, 460 nm and 645 nm, which correspond to anatase TiO_2, $TiO_2/ZnFe_2O_4$/AFAC sample and the $ZnFe_2O_4$ material, respectively. On further addition of AFAC, the light absorption of $TiO_2/ZnFe_2O_4$/AFAC sample slightly enhanced. Based on the optical absorption edge obtained from UV-DRS, the energy band gaps for direct band-gap semiconductor of different samples were calculated by plotting $(Ahv)^{1/2}$ to hv,[6,27,37] where A is the absorption coefficient, hv is the photon energy and E_g is the energy band gap; the measured energy band gap values of the samples are listed in Table 1. The estimated E_g values of the as-prepared $ZnFe_2O_4$, $TiO_2/ZnFe_2O_4$, $TiO_2/ZnFe_2O_4$/0.02 g AFAC and $TiO_2/ZnFe_2O_4$/0.30 g AFAC samples were 1.33 eV, 2.56 eV, 2.50 eV and 2.44 eV, respectively, which indicated that all the above samples would possess photocatalytic ability under visible light irradiation. The energy band-gap of anatase TiO_2 is 3.18 eV; when hybridized with 0.35 g narrow band-gap semiconductor $ZnFe_2O_4$, it decreases greatly to 2.56 eV in $TiO_2/ZnFe_2O_4$ nanocomposite, which is similar to previous reports.[17–21] When hybridized with 0.30 g AFAC, the band-gap decreases to 2.44 eV, which had a less significant effect on the band-gap than that reported by Huo *et al.*[6] Hence, $ZnFe_2O_4$ has more influence on the band gap of TiO_2 than that of AFAC in our as-prepared $TiO_2/ZnFe_2O_4$/AFAC photocatalysts. The visible red shift of the adsorption of $TiO_2/ZnFe_2O_4$/AFAC samples resulted from two factors. One factor was the mixing effect of band gaps of $ZnFe_2O_4$ and TiO_2 semiconductors discussed above. Since the added amount of $ZnFe_2O_4$ was small (3 wt%), the mixing effect alone cannot account for the entire large red shift. The other factor considered was the interface effect. Due to the interfacial coupling effect between $ZnFe_2O_4$ and TiO_2 grains, $ZnFe_2O_4$ can induce lattice defects on the

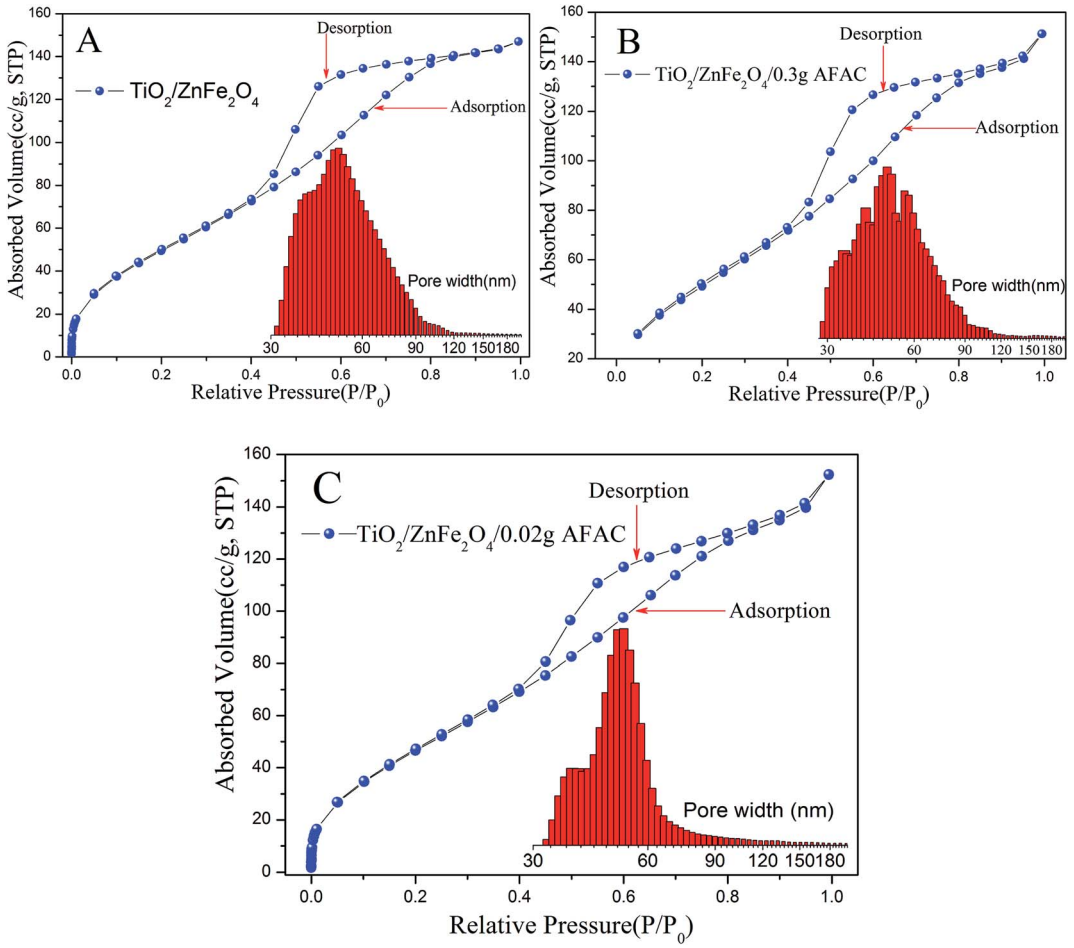

Fig. 4 BET isotherm and pore diameter distribution of different samples: (A) $TiO_2/ZnFe_2O_4$; (B) $TiO_2/ZnFe_2O_4$/0.30 g AFAC; (C) $TiO_2/ZnFe_2O_4$/0.02 g AFAC (inset illustrates the graph of the corresponding pore diameter distributions).

Table 2 BET specific surface area of different samples

Sample	Pore volume ($cm^3\ g^{-1}$)	BET specific surface ($m^2\ g^{-1}$)	Half pore width (nm)	Fitting error
$TiO_2/ZnFe_2O_4$	0.213	162.183	25.935	2.495%
$TiO_2/ZnFe_2O_4$/0.02 g AFAC	0.209	151.122	24.210	2.618%
$TiO_2/ZnFe_2O_4$/0.30 g AFAC	0.219	167.447	26.500	0.474%

surface TiO_6 octahedra, which may serve as the centers of bound excitons.[38] These two factors together resulted in the red shift of the band gap of $TiO_2/ZnFe_2O_4$/AFAC photocatalysts.

3.5 Adsorption of RhB

The adsorption ability would affect the photocatalysis performance greatly. Hence, rhodamine B (RhB) was chosen as the simulated pollutant to evaluate the adsorption activity of the as-prepared photocatalysts. Fig. 6A shows the adsorption process of RhB removal on different $TiO_2/ZnFe_2O_4$/AFAC photocatalysts in the dark for 120 min; all the samples adsorbed the RhB quickly in the first 15 min and achieved maximum adsorption after 30 min. Their adsorption kinetics of RhB shown in Fig. 6B could be fitted well with a pseudo-second-order adsorption model.[27] The adsorption pseudo second-order kinetic constants (k_2) and their standard error, and the regression coefficient R^2 are listed in Table 3. Therefore, the photocatalysts were first placed in dark for 30 min to reach the adsorption equilibrium and then were irradiated by the Xe lamp for 75 min for photocatalytic degradation. It was noteworthy that the adsorption activity of $TiO_2/ZnFe_2O_4$/0.30 g AFAC photocatalyst was not even as good as that of the $TiO_2/ZnFe_2O_4$ nanocomposite, which would result in disadvantageous influence on the final removal rate of RhB.

3.6 Photocatalytic degradation of RhB

The photocatalytic activity of the pristine TiO_2, $TiO_2/ZnFe_2O_4$, $TiO_2/ZnFe_2O_4$/0.02 g AFAC and $TiO_2/ZnFe_2O_4$/0.30 g AFAC were evaluated by degrading RhB under visible light, simulated sunlight (without the 420 nm cutoff filter) and UV light irradiation. The results are shown in Fig. S1.† Under UV light irradiation, RhB was almost thoroughly degraded in 15 min by pure TiO_2; however, it was evident that TiO_2 was impotent for the

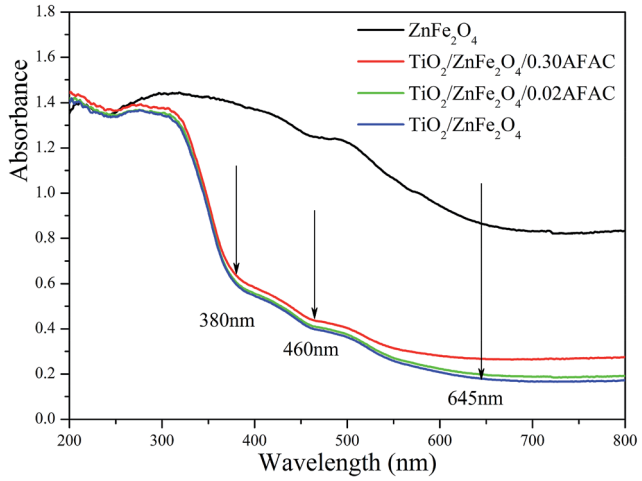

Fig. 5 UV-vis DRS of $ZnFe_2O_4$, $TiO_2/ZnFe_2O_4$, $TiO_2/ZnFe_2O_4$/0.02 g AFAC and $TiO_2/ZnFe_2O_4$/0.30 g AFAC samples.

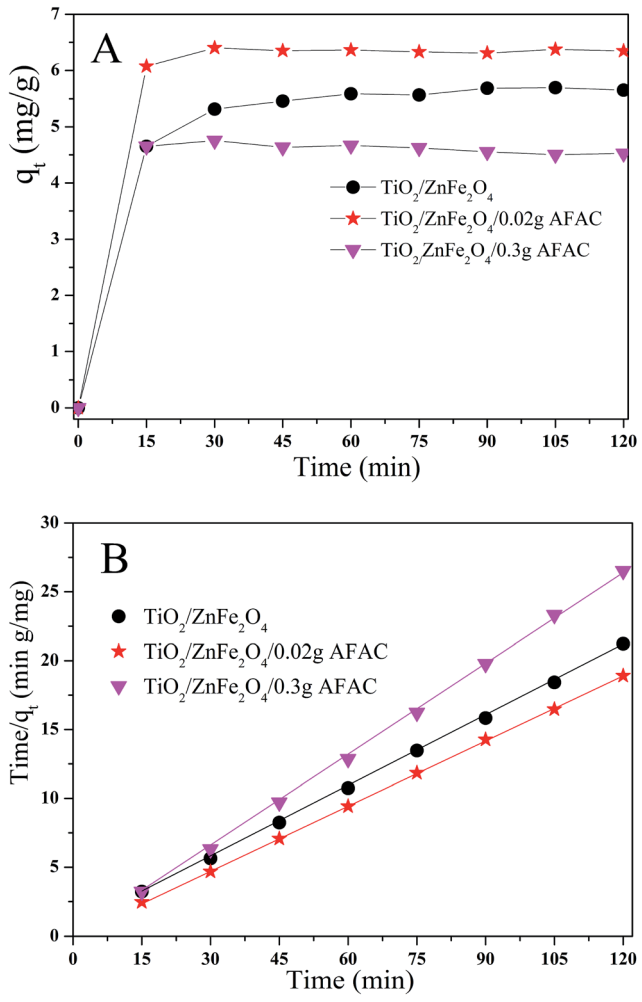

Fig. 6 (A) Adsorption kinetics of RhB onto $TiO_2/ZnFe_2O_4$ nanocomposite, $TiO_2/ZnFe_2O_4$/0.02 g AFAC and $TiO_2/ZnFe_2O_4$/0.30 g AFAC photocatalysts; (B) pseudo second-order kinetic plots for RhB removal.

Table 3 Adsorption pseudo second-order kinetic constant and related parameters of different samples

Samples	k_2 (g mg^{-1})	Standard error	R^2
$TiO_2/ZnFe_2O_4$	0.14284	0.00611	0.98732
$TiO_2/ZnFe_2O_4$/0.02 g AFAC	0.15692	0.00152	0.99935
$TiO_2/ZnFe_2O_4$/0.30 g AFAC	0.20229	0.00333	0.99810

degradation of RhB under visible light irradiation. Hence, we focused on the photocatalytic performance of the as-prepared composites under visible light, which would be enlightening for future application. Fig. 7 shows the processes of RhB removal on different $TiO_2/ZnFe_2O_4$/AFAC photocatalysts under visible light irradiation. The $TiO_2/ZnFe_2O_4$ nanocomposite removed 95.1% of the RhB. When hybridized with 0.02 g AFAC, the $TiO_2/ZnFe_2O_4$/0.02 g AFAC photocatalyst removed 97.1% of the RhB with the highest photocatalytic rate except for the abnormal upturn point located at 30 min, which is demonstrated in Fig. 8. When the amount of AFAC was increased to 0.30 g, the ratio of the removed RhB decreased to 91%, which resulted from its relatively weak adsorption activity of RhB as mentioned before. With the appropriate band gap, large specific surface area and good adsorption ability, the $TiO_2/ZnFe_2O_4$/0.02 g AFAC photocatalyst had the best photocatalytic performance on the degradation of RhB among all our samples.

RhB could hardly be photodegraded under visible light irradiation;[39] therefore the removal of RhB was primarily attributed to the photocatalytic degradation by the photocatalyst. Fig. 8 shows the spectra of photocatalytic degradation of RhB by the three photocatalysts. When the simulated RhB wastewater was irradiated under visible light, RhB was clearly photodegraded in 75 min. The color of the wastewater changed gradually from magenta to colorless (Fig. 8A). The maximum absorption peak shifted gradually from 552 nm to 495 nm, which implied that there were different intermediate products. Under visible light irradiation, the $TiO_2/ZnFe_2O_4$

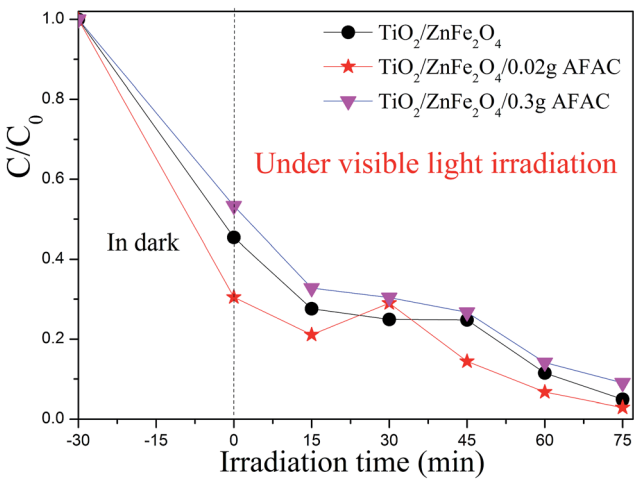

Fig. 7 The photodegradation rate of RhB with different photocatalysts under visible light.

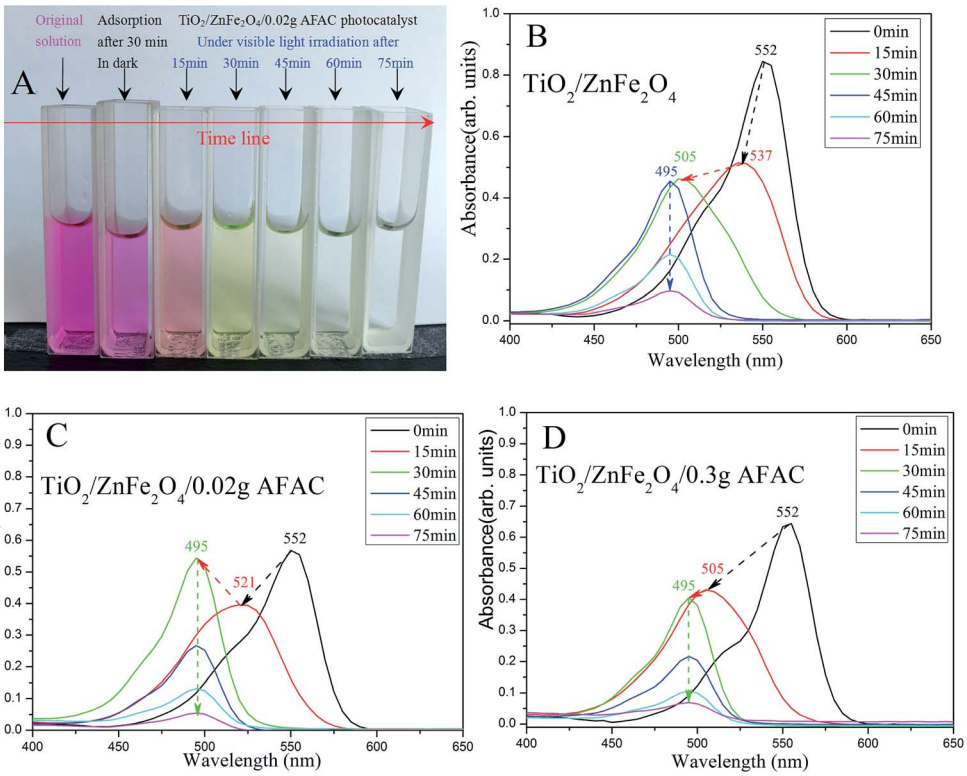

Fig. 8 (A) The color of the simulated wastewater after different times under visible light by $TiO_2/ZnFe_2O_4$/0.02 g AFAC photocatalyst; the spectra of photocatalytic degradation of RhB by (B) $TiO_2/ZnFe_2O_4$; (C) $TiO_2/ZnFe_2O_4$/0.02 g AFAC and (D) $TiO_2/ZnFe_2O_4$/0.30 g AFAC photocatalysts.

nanocomposite first photodegraded RhB (550 nm) to *N*,*N*,*N*′-triethyl rhodamine (537 nm) after 15 min, then to rhodamine (495 nm) after 30 min and the peak of rhodamine sharply decreased after 75 min, which indicated that RhB was photodegraded. Moreover, the $TiO_2/ZnFe_2O_4$/0.02 g AFAC photocatalyst photodegraded RhB (550 nm) first to *N*,*N*′-diethyl rhodamine (521 nm) after 15 min and then to rhodamine (495 nm) after 30 min. The $TiO_2/ZnFe_2O_4$/0.30 g AFAC photocatalyst photodegraded RhB (550 nm) first to *N*-ethyl rhodamine (505 nm) after 15 min and then to rhodamine (495 nm) after 30 min. The above results were similar to those reported by Watanabe *et al.*,[40] in which the absorption of the intermediate products changed from RhB (555 nm), to *N*,*N*,*N*′-triethyl rhodamine (539 nm), *N*,*N*′-diethyl rhodamine (522 nm), *N*-ethyl rhodamine (510 nm) and rhodamine (498 nm). Fig. 8C shows an abnormal upturn from *N*,*N*′-diethyl rhodamine (521 nm) to rhodamine (495 nm) after 30 min, corresponding to the abnormal upturn of the $TiO_2/ZnFe_2O_4$/0.02 g AFAC photocatalyst (Fig. 7), which implied that the formation of rhodamine (495 nm) was critical to the photocatalysis process.

The process of RhB removal on the $ZnFe_2O_4/TiO_2$/AFAC photocatalyst surface could be summarized as follows: (1) when the $ZnFe_2O_4/TiO_2$ nanocomposite was loaded on AFAC, the surface adsorption of RhB on the photocatalyst could be enhanced, which causes a concentration effect in photodegrading RhB; (2) the photodegradation of RhB would empty the adsorption sites on the surface of the photocatalyst, which would continue adsorbing molecular RhB. The synergistic effects of the adsorption ability and photocatalytic ability of the $ZnFe_2O_4/TiO_2$/AFAC photocatalyst improve the removal of RhB in the solution.

3.7 Recyclability

To evaluate the recyclability of the as-prepared catalysts, the $ZnFe_2O_4/TiO_2$/0.02 g AFAC photocatalyst was selected to test the recycle experiments. As shown in Fig. 9, after two and three runs, about 83.4% and 73.7% of RhB was photodegraded, respectively. The photocatalytic performance of the as-prepared catalyst decreased slightly during the photodegradation process. The decrease in the RhB removal efficiency might be attributed to the accumulation of RhB on the photocatalyst surface, which blocked the mesopores gradually, and then the adsorption of RhB from the solution was restrained. Therefore, to improve the photocatalytic performance of the reused catalyst, appropriate prolonging of the oxidation time is beneficial.

3.8 Photocatalytic mechanism

Under visible light, the impressive photocatalytic performance of the $ZnFe_2O_4/TiO_2$/0.02 g AFAC photocatalyst primarily resulted from the following three factors: (1) the crystallite size of the as-prepared anatase TiO_2 was less than 10 nm, which indicated that the specific surface area of anatase TiO_2 would be large; (2) when TiO_2 particles were coated on $ZnFe_2O_4$ particles, the band-gap of the $TiO_2/ZnFe_2O_4$ nanocomposite decreased from 3.18 to 2.56 eV, so the nanocomposite could photodegrade

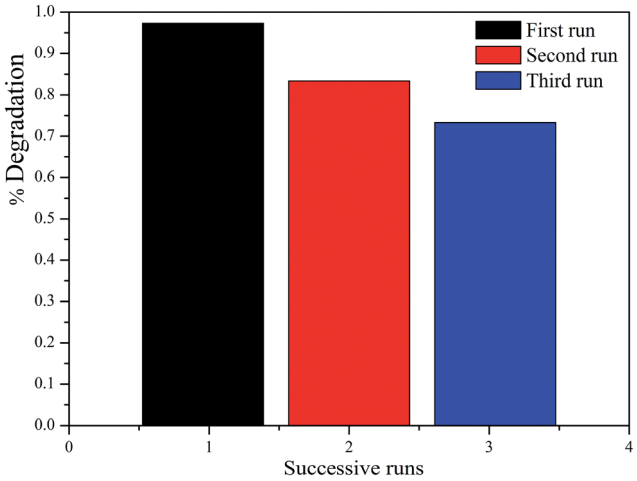

Fig. 9 The photocatalytic degradation of RhB for three cycles by TiO_2/$ZnFe_2O_4$/0.02 g AFAC photocatalyst.

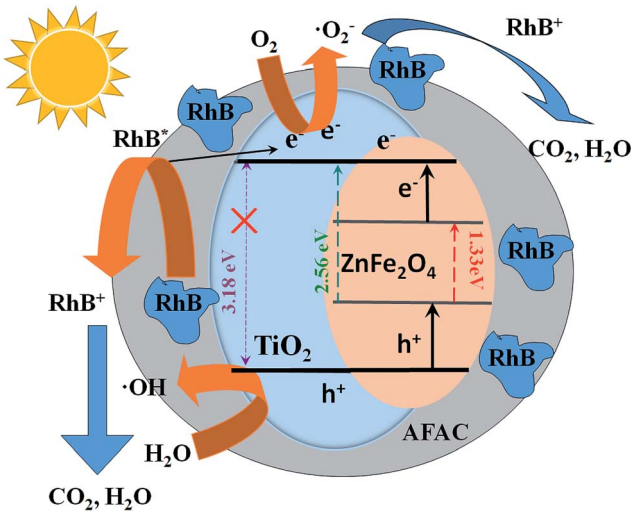

Fig. 10 Schematic diagram of photocatalytic degradation of RhB on TiO_2/$ZnFe_2O_4$/AFAC photocatalyst under visible light irradiation.

RhB under visible light irradiation; (3) when hybridized with 0.02 g AFAC, the TiO_2/$ZnFe_2O_4$/0.02 g AFAC exhibited a band-gap of 2.50 eV, the number of the macropores in the photocatalyst decreased and the majority of the pores were mesopores, which resulted in a competitive phenomenon: a dominant positive effect of the enhancement of the adsorption ability and a negligible negative effect of a decrease in the specific surface area from 162.18 $m^2\ g^{-1}$ to 151.12 $m^2\ g^{-1}$. The combination of the above three positive factors resulted in a synergistic effect, which led to the slight enhancement of the photocatalytic performance from 95% to 97.1%. When hybridized with 0.30 g AFAC, although the TiO_2/$ZnFe_2O_4$/0.30 g AFAC photocatalyst had a bigger specific surface area of 167.44 $m^2\ g^{-1}$ and a smaller band-gap of 2.44 eV, which were both positive effects for photocatalytic performance, the removal efficiency of RhB decreased to 91%. The reason might be as follows: the more AFAC was added, the more chances that AFAC may absorb and reflect the visible light energy, so less energy would be absorbed by the TiO_2/$ZnFe_2O_4$ photocatalyst and eventually the photocatalytic performance decreased.

A probable photocatalytic mechanism is schematically illustrated in Fig. 10. Under visible light irradiation, the electrons (e^-) would be promoted to the conduction band (CB), while some corresponding positive holes (h^+) would emerge in the valence band (VB) as described in eqn (1).[16,41,42] The photogenerated electrons could migrate to the surface and adsorb molecular oxygen to generate the superoxide radical ($^{\bullet}O_2^-$) (eqn (2)) and the photogenerated holes could react with the adsorbed H_2O molecules to generate hydroxyl radical ($^{\bullet}OH$) (eqn (3)).[43] The RhB adsorbed on the photocatalyst surface could be promoted to its excited state (RhB*);[44] then, RhB* would promote an electron to the photocatalyst and $^{\bullet}RhB^+$ would be formed (eqn (4)). The generated superoxide radicals, hydroxyl radicals and the photogenerated holes of the valence band could degrade RhB (and $^{\bullet}RhB^+$) into carbon dioxide and water (eqn (5)). The above process can be summarized as follows:

$$ZnFe_2O_4/TiO_2/AFAC + h\nu \rightarrow e^- + h^+ \quad (1)$$

$$e^- + O_2 \rightarrow {}^{\bullet}O_2^- \quad (2)$$

$$h^+ + H_2O \rightarrow {}^{\bullet}OH + {}^{\bullet}H \quad (3)$$

$$RhB + h\nu \rightarrow RhB^* \rightarrow {}^{\bullet}RhB^+ + e^- \quad (4)$$

$$h^+, {}^{\bullet}O_2^-, {}^{\bullet}OH + RhB, {}^{\bullet}RhB^+ \rightarrow N,N,N'\text{-triethyl rhodamine} \rightarrow N,N'\text{-diethyl rhodamine} \rightarrow N\text{-ethyl rhodamine} \rightarrow \text{rhodamine} \rightarrow CO_2, H_2O, \textit{etc.} \quad (5)$$

4. Conclusions

A series of TiO_2/$ZnFe_2O_4$/AFAC photocatalysts were prepared on the basis of the sol–gel and hydrothermal method. By coating $ZnFe_2O_4$ nanoparticles with TiO_2 nanoparticles, the band gap of TiO_2/$ZnFe_2O_4$ nanocomposite was narrowed to 2.56 eV, which would possess photocatalytic ability under visible light. When the AFAC was hybridized with the TiO_2/$ZnFe_2O_4$ nanocomposite, their adsorption capacity and absorption ability were enhanced. Under visible light irradiation for 75 min, the removal rate of RhB on the TiO_2/$ZnFe_2O_4$ nanocomposite and TiO_2/$ZnFe_2O_4$/0.02 g AFAC photocatalyst were 95.0% and 97.1%. However, on hybridization with more AFAC, the TiO_2/$ZnFe_2O_4$/0.30 g AFAC photocatalyst had a lower removal rate of 91%. The impressive photocatalytic performance originated from the synergistic effect of small crystallite size, narrow band-gap and mesoporous structure of the photocatalysts. Recycling experiments indicated that the photocatalyst retained higher activity after three cycles. Therefore, the TiO_2/$ZnFe_2O_4$/AFAC photocatalysts would have potential application in environmental remediation.

Conflicts of interest

There are no conflicts to declare.

Acknowledgements

This work was supported by National Natural Science Foundation of China (Grant No. 61775081, 61475063, 21576111) and the Graduate Innovation Research Fund at the Jilin Normal University (No. 201628).

References

1 A. Fujishima, T. N. Rao and D. A. Tryk, *J. Photochem. Photobiol., C*, 2000, **1**, 1–21.
2 A. Fujishima, X. T. Zhang and D. A. Tryk, *Surf. Sci. Rep.*, 2008, **63**, 515–582.
3 Y. Su, P. Chen, F. Wang, *et al.*, *RSC Adv.*, 2017, **7**(54), 34096–34103.
4 Y. L. Pang and A. Z. Abdullah, *J. Hazard. Mater.*, 2012, **235**, 326–335.
5 J. Lim, A. D. Bokare and W. Choi, *RSC Adv.*, 2017, **7**(52), 32488–32495.
6 P. Huo, Y. Yan, S. Li, H. Li and W. Huang, *Desalination*, 2010, **263**, 258–263.
7 S. G. Kumar and L. G. Devi, *J. Phys. Chem. A*, 2011, **115**, 13211–13241.
8 L. G. Gao, J. W. Du and T. L. Ma, *Ceram. Int.*, 2017, **43**(12), 9559–9563.
9 J. Li, S. Jia, G. Sui, *et al.*, *RSC Adv.*, 2017, **7**(55), 34857–34865.
10 M. Xing, Y. Wu, J. Zhang and F. Chen, *Nanoscale*, 2010, **2**, 1233–1239.
11 M. Kang, *J. Mol. Catal. A: Chem.*, 2003, **197**, 173–183.
12 F. Magalhães, F. C. Moura and R. M. Lago, *Desalination*, 2011, **276**, 266–271.
13 Q. Zhu, X. H. Hu, M. S. Stanislaus, N. Zhang, R. D. Xiao, N. Liu and Y. N. Yang, *Sci. Total Environ.*, 2017, **577**, 236–244.
14 S. Y. Guo, J. G. Dai, T. J. Zhao, *et al.*, *RSC Adv.*, 2017, **7**(58), 36787–36792.
15 G. Li, X. Nie, J. Chen, Q. Jiang, T. An, P. K. Wong, H. Zhang, H. Zhao and H. Yamashita, *Water Res.*, 2015, **86**, 17–24.
16 P. Cheng, C. Deng, M. Gu and W. Shangguan, *J. Mater. Sci.*, 2007, **42**(22), 9239–9244.
17 Z. Yuan and L. Zhang, *J. Mater. Chem.*, 2001, **11**(4), 1265–1268.
18 H. Yang, X. Y. Li, Q. D. Zhao, X. Quan and G. H. Chen, *Environ. Sci. Technol.*, 2010, **44**(13), 5098–5103.
19 Y. Hou, X. Y. Li and Q. D. Zhao, *Adv. Funct. Mater.*, 2010, **20**(13), 2165–2174.
20 E. Moreira, L. A. Fraga and M. H. Mendonça, *J. Nanopart. Res.*, 2012, **14**(6), 1–10.
21 M. Wang, L. Sun and J. Cai, *J. Mater. Chem. A*, 2013, **1**(39), 12082–12087.
22 J. Zhang, X. Wang, X. Wang, J. Song, J. Huang, B. Louangsouphom and J. Zhao, *RSC Adv.*, 2015, **5**, 71922–71931.
23 X. Wang, W. Wang, X. Wang, J. Zhang, Z. Gu, L. Zhou and J. Zhao, *Appl. Surf. Sci.*, 2015, **349**, 264–271.
24 S. Hosseini, S. Borghei, M. Vossoughi and N. Taghavinia, *Appl. Catal., B*, 2007, **74**, 53–62.
25 L. C. R. Machado, C. B. Torchia and R. M. Lago, *Catal. Commun.*, 2006, **7**, 538–541.
26 B. Wang, C. Li, J. Pang, X. Qing, J. Zhai and Q. Li, *Appl. Surf. Sci.*, 2012, **258**, 9989–9996.
27 J. Song, X. J. Wang, Y. J. Bu, X. Wang, J. Zhang, J. Y. Huang, R. R. Ma and J. F. Zhao, *Appl. Surf. Sci.*, 2017, **391**, 236–250.
28 A. N. Ökte and D. Karamanis, *Appl. Catal., B*, 2013, **142**, 538–552.
29 A. Dagar and A. K. Narula, *J. Mater. Sci.: Mater. Electron.*, 2017, **28**(12), 8643–8654.
30 Y. Ao, J. Xu and D. Fu, *Sep. Purif. Technol.*, 2008, **61**(3), 436–441.
31 C. G. Anchieta, A. Cancelier, M. A. Mazutti, *et al.*, *Materials*, 2014, **7**(9), 6281–6290.
32 N. Dhiman, B. P. Singh and A. K. Gathania, *J. Nanophotonics*, 2012, **6**(1), 063511-1–063511-10.
33 C. Yang, T. Wang and P. Liu, *Curr. Opin. Solid State Mater. Sci.*, 2009, **13**(5), 112–118.
34 M. Donohue and G. Aranovich, *Adv. Colloid Interface Sci.*, 1998, **76**, 137–152.
35 M. Kruk and M. Jaroniec, *Chem. Mater.*, 2001, **13**(10), 3169–3183.
36 Z. Jing and J. Zhan, *Adv. Mater.*, 2008, **20**, 4547–4551.
37 S. Delekar, H. Yadav, S. Achary, S. Meena and S. Pawar, *Appl. Surf. Sci.*, 2012, **263**, 536–545.
38 L. V. Saraf, S. L. Patil and S. B. Ogale, *J. Mod. Phys.*, 1998, **12**(25), 2635–2647.
39 X. Wang, X. Wang, J. Zhao, J. Chen, J. Zhang, J. Song and J. Huang, *RSC Adv.*, 2015, **5**, 66611–66620.
40 T. Watanabe, T. Takirawa and K. Honda, *J. Phys. Chem.*, 1977, **81**, 1845–1851.
41 E. Moreira, L. A. Fraga, M. H. Mendonça, *et al.*, *J. Nanopart. Res.*, 2012, **14**(6), 937.
42 I. Kryuko, S. Y. Kuchmii and V. D. Pokhodenko, *Theor. Exp. Chem.*, 2000, **36**(2), 63–81.
43 L. G. Devi and S. G. Kumar, *Appl. Surf. Sci.*, 2011, **257**, 2779–2790.
44 H. Wang, X. Yuan, Y. Wu, G. Zeng, X. Chen, L. Leng and H. Li, *Appl. Catal., B*, 2015, **174**, 445–454.